Optics & Laser Technology 203 (2026) 115596

Contents lists available at ScienceDirect

Optics and Laser Technology

journal homepage: www.elsevier.com/locate/optlastec

Synchrotron radiation imaging-based understanding of spatter reduction condition in laser beam keyhole welding of austenitic stainless steels through superimposed intensities☆

Christian Diegel [a,*], Leander Schmidt [a], Klaus Schricker [a,b], Marc Seibold [a], Felix Zaiß [c], Christian Hagenlocher [c], Christoph Spurk [d], Marc Hummel [d,e], Alexander Olowinsky [e], Felix Beckmann [f], Julian Moosmann [f], Thomas Graf [c], Jean Pierre Bergmann [a]

[a] Technische Universität Ilmenau, Production Technology Group, Ilmenau, Germany
[b] Brandenburg University of Technology Cottbus-Senftenberg, Chair of Joining and Welding Technology, Cottbus, Germany
[c] University of Stuttgart, Institut für Strahlwerkzeuge (IFSW), Stuttgart, Germany
[d] RWTH Aachen University, Chair for Laser Technology LLT, Aachen, Germany
[e] Fraunhofer Institute for Laser Technology ILT, Aachen, Germany
[f] Institute of Material Physics, Helmholtz-Zentrum Hereon, Geesthacht, Germany

ARTICLE INFO

Keywords:
Laser welding
Spatter formation
High-speed synchrotron radiation imaging in situ X-ray
Intensity distribution
Melt flows

ABSTRACT

High welding speeds above 8 m/min during laser beam welding of high-alloy steel lead to spatter formation, resulting in material losses and spatter adhesion that significantly degrade seam quality. Superimposing the main laser intensity with a second laser intensity leads to a reduction of such effects, as melt flow conditions around the keyhole are influenced. In this configuration, the area hit from the superimposed laser must be notably larger than the main laser spot, in order to enlarge the melt pool on the top side. However, the basic interactions of keyhole, melt pool, and metal vapor using a superimposed intensity are largely unknown.

In order to identify and understand the related effects with combined laser intensities a welding speed of 12 m/min was chosen, while through high-speed synchrotron radiation imaging visualization of keyhole behavior and melt flow characteristics by tracking tungsten carbide particles was carried out. The superimposed intensity widens the melt pool on the sheet top side, thereby increasing the cross-sectional area of the melt flow, while the keyhole geometry and its fluctuations remain comparable to those observed without superimposed intensity. This reduces the melts kinetic energy of the flow around the keyhole and finally spatter formation. Raising power of the superimposed laser intensity, the keyhole width expands over its entire depth, and a bulge on the keyhole rear wall due to vaporizing material is formed. This bulge causes fluctuations of the melt pool and leads to lateral spatter formation due to an upward directed melt flow at the keyhole walls. Therefore, in order to reduce spatter formation, the power of the superimposed intensity has to be chosen consequently in order to enhance melt pool dimensions and avoid bulging.

1. Introduction

Laser beam welding (LBW) is used for a wide range of various industrial applications. In particular, continuous wave (cw) keyhole mode welding enables high penetration depths and narrow weld seams [1]. Furthermore, the increasing laser beam power of modern solid–state lasers [2] enables welding speeds above 10 m/min for manufacturing steel structures [3]. Higher welding speeds shorten manufacturing processes, reduce cycle times, and increase the efficiency of industrial production processes [4]. However, higher welding speeds lead to a significant number of spatter for joining high–alloy steel components [5]. Spatter formation leads to a loss of mass [6] and a reduced cross–section of the weld [7]. Resulting undercuts weaken the cross-section of the weld seam for mechanical load and can be a reason for a rejection of the welded component [8]. Contaminants can also accumulate at the weld seam due to undercuts or adhering spatter and effect the

☆ This article is part of a special issue entitled: 'LIM 2025' published in Optics and Laser Technology.

* Corresponding author at: Gustav-Kirchhoff-Platz 2, 98693 Ilmenau, Germany.
E-mail address: christian.diegel@tu-ilmenau.de (C. Diegel).

https://doi.org/10.1016/j.optlastec.2026.115596
Received 10 October 2025; Received in revised form 23 February 2026; Accepted 8 April 2026
Available online 2 June 2026
0030-3992/© 2026 The Author(s). Published by Elsevier Ltd. This is an open access article under the CC BY license (http://creativecommons.org/licenses/by/4.0/).

cleanability of the welded part [9]. This is particularly relevant in the food, medical, and chemical industry [10], where the use of high-alloy steel components is required due to their oxidation resistance [11]. In addition, costly rework is required to remove spatter adhesions due to optical concerns [12]. Therefore, one objective when laser welding of austenitic high-alloy steel is to avoid spatter, to improve the quality of the welded component and avoid costly rework. Superposition of a further laser intensity forming an intensity distribution differing from typical Gaussian or tophat distribution seems to be a promising way, leading to reduced spatter formation [13]. Even though the potentials were demonstrated, the effects are not fully understood at the moment.

Numerous publications already describe the effect of welding speed on keyhole, melt pool, and metal vapor behavior. Mainly it can be concluded, that the laser welding process can be subdivided in different process regimes depending on the welding speed. The effect of welding speeds is highlighted in literature by [14], even though the different regimes can shift depending on experimental conditions. According to [14] welding speeds below 5 m/min lead to small spatter detachments undirected from the keyhole rim. This phenomenon is described to be typical of a so called "Rosenthal regime" [15]. Increasing welding speed (6 m/min [16] to 10 m/min [17]) leads to a peculiar spatter formation condition, where spatter form from melt swellings at the keyhole rear wall [16] (see Fig. 1). Such a condition is referred to as the "single wave regime" [14]. By increasing welding speeds from 9 m/min to 16 m/min [14], the keyhole extension in welding direction enhances and is referred to as the "elongated keyhole regime". Within this regime, spatter continuously detach from the melt swelling immediately behind of the keyhole rear wall [18].

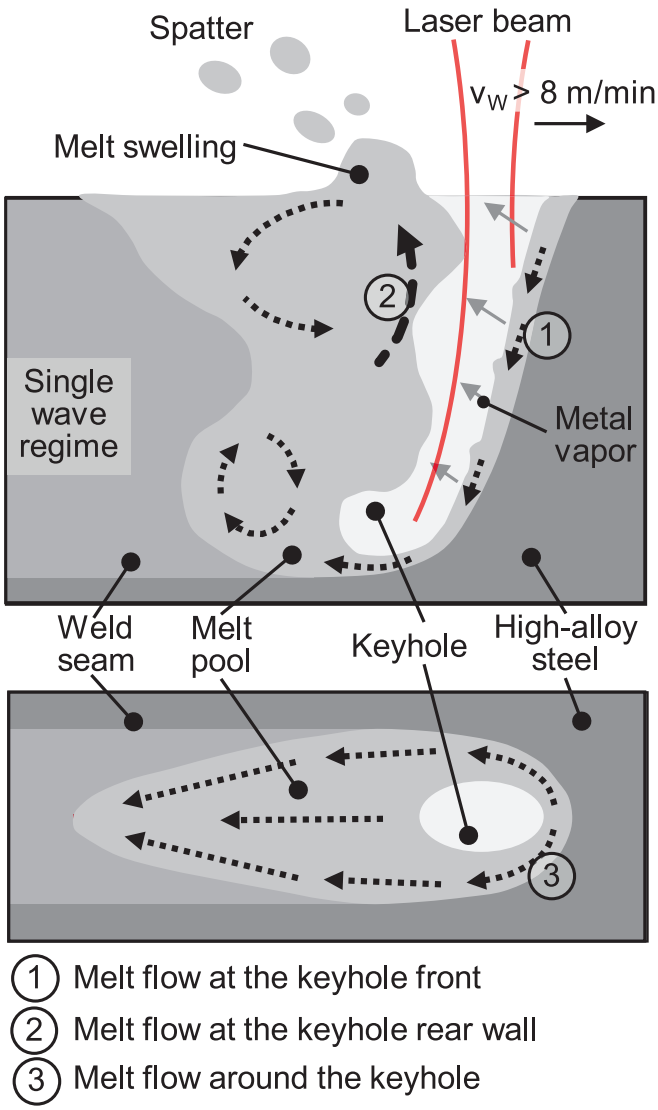


Fig. 1. Schematic illustration of the relevant melt flows for spatter formation during keyhole welding.

In addition to the regime descriptions, investigating the various conditions for a spatter formation is highly relevant to clarify the changes in spatter formation with increasing welding speed. In order to reach spatter detachment, the kinetic energy of a fluid element $E_{kin,fl}$ resulting in the detachment of a spatter should be equal or higher than the sum of the kinetic energy $E_{kin,sp}$ and the surface energy E_{sur} to form a spatter (see Equation (1)) [19]. The kinetic energies are calculated using melt density ρ, spatter volume V_{sp}, spatter velocity v_{sp}, and melt flow velocity v_{fl} [20]. Surface tension σ and spatter surface S_{sp} determine the surface energy E_{sur} [21]. This results in the following condition for a spatter formation [19]:

$$\underbrace{\rho V_{sp} v_{fl}^2}_{E_{kin,fl}} \geq \underbrace{\rho V_{sp} v_{sp}^2}_{E_{kin,sp}} + \underbrace{2\sigma S_{sp}}_{E_{sur}}. \quad (1)$$

Therefore, spatter formation is mainly determined by the local surface tension σ of the melt and the local melt flow velocity v_{fl} at the detachment site. These conditions are a result of the different melt flows around the keyhole as well. Surface tension depends mainly on material composition and temperature of the melt as well as interactions with the gas [22]. The temperature dependency of the material leads in the melt pool to a surface tension gradient, that results in a convection flow called Marangoni flow [23]. However, the effect of the Marangoni flow on spatter formation can be neglected using higher welding speeds v_w (> 8 m/min) [24]. In addition to the Marangoni flow in the melt pool, principally three further regional conditions determine the global melt flow. At first in the region of the keyhole front wall the melt flow is directed downwards, accelerated by the recoil pressure of local evaporation on the surface of small humps on the keyhole front [25] (see Fig. 1, melt flow 1). The metal vapor is formed from the interaction of the laser beam with the keyhole walls, especially on the keyhole front. The metal vapor is directed upwards, escaping from the keyhole area. This escaping vapor accelerates the melt on the keyhole rear wall [26] (see Fig. 1, melt flow 2). Furthermore, material melted in front of the keyhole must flow around the aperture over the complete height of it due to the feed rate of the laser beam [27] (see Fig. 1, melt flow 3). This flow component increases particularly with higher welding speeds [26].

The upward melt flow at the keyhole rear wall mainly determines the melt flow velocity in the condition for a spatter formation for welding speeds up to 6 m/min [24]. However, the undirected spatter formation for low welding speeds is relatively minor compared to a directed detachment of spatter with trajectories in the opposite welding direction out of the melt swelling at higher speeds [7]. Although the upward melt flow velocity remains constant as the welding speed increases, the effect of the melt flow around the keyhole on spatter formation increases significantly with the welding speed [26]. With regard to a model assumption the maximum velocity was assumed in [26] being proportional to the welding speed with an exponent of approx. 1,5 ($v_{fl} \propto v_w^{1.5}$). The highest melt flow velocity is determined at the liquid–vapor interface and decreases with increasing distance from the keyhole. For example, a calculation of the melt flow of pure iron results in a maximum flow velocity of 1.5 m/s for a welding speed of 12 m/min and 2.3 m/s for 18 m/min [26].

In general, adjustments of the welding processes are required to effectively reduce the spatter formation from the melt swellings behind the keyhole aperture. Beam shaping using coherent beam combining [28], a concentric intensity distribution [29], and an additional intensity distribution from two laser sources [30] are promising for process improvement. In particular, the superposition of a spot for keyhole formation with a comparatively larger spot to increase the melt pool

around the keyhole reduces the spatter formation by up to 80% [31]. This process improvement was attributed to a reduction in the melt flow velocity of the flow around the keyhole, according to the continuity equation and, thereby reducing the kinetic energy of the melt [13]. However, this hypothesis in the literature has not yet been experimentally verified and therefore requires further investigation. Consequently, measuring the melt flow velocities in correlation with the keyhole behavior remains pending and is essential for validating existing assumptions and improving the knowledge about the correlation between melt flow dynamics and spatter formation. Nevertheless, it is also crucial to understand the effect of different intensity distributions in order to develop new laser beam sources or beam-shaping elements for welding applications. Suitable methods are required to measure these flow velocities, which are outlined in the following.

In addition to keyhole front observations and process simulations [32], experimental investigations using tracer particles in X-ray imaging and half-section setup are reported in literature. Tungsten carbide particles are used for this purpose [33] due to their high melting temperature and density compared to high-alloy steel [34]. Notably, the X-ray imaging enables an in situ investigation of the keyhole and melt pool behavior with a negligible effect on the general process effects regarding e.g. keyhole dynamics or pore formation [35]. To observe these process effects, frame rates of up to 100,000 images/second are achievable during welding of high-alloy steel [36]. Therefore, X-ray imaging using tracer particles during the welding process provides a suitable method for investigating melt flows. The two-dimensional projection of the three-dimensional melt flows must be considered during the evaluation and will be addressed in the investigation.

2. Materials and methods

2.1. Material and geometry of the specimen

Welding experiments were carried out on laser-cut specimens of high-alloy steel. Table 1 provides information on the chemical composition, which was determined using a scanning electron microscope (JEOL JSM-IT800HT) and energy dispersive X-ray spectroscopy (EDS) for the measurement of the iron (Fe), chromium (Cr), nickel (Ni) and manganese (Mn) composition. A wavelength dispersive X-ray Spectroscopy (WDS) measurement determined the silicon (Si), phosphorus (P) and sulfur (S) composition, as these elements predominantly affect surface tension. The measurements were performed on the top side of an exemplary sheet at two different locations with a distance of 10 mm. Each location covered an area of 200 µm x 250 µm. Within these areas, 10 measurement spots were randomly distributed at a distance of approx. 50 µm from each other, resulting in a total of 20 measurements. The following values are derived from these 20 measurements.

Even though the sheets are nominally AISI 304, nevertheless the measured values are at the limits of the intervals defined by the standards in [37]. The nickel content is at the lower limit of the permissible range (min. 8 wt–%), while the silicon content is at the upper limit (max. 1 wt–%). The combined mass fraction of the other elements (carbon and nitrogen) is limited to 0.17 wt-%, but the other measured values exceed this threshold. Due to the elevated silicon content, the composition more closely corresponds to AISI 301. However, even in this case, the other elements exceed the maximum permitted value of 0.25 wt–%. Previous studies demonstrate that alloying elements can affect the spatter formation during laser beam welding [38]. Nevertheless, a deviation in the chemical composition from the specified material does not influence the validity of the present results, as long as the material is not altered during the experiments. In addition, the mechanisms outlined in the following are consistent with findings reported in various publication on laser beam welding of AISI 304.

Table 1
Average composition with standard deviation for the used high alloy steel in wt.-%.

Fe	Cr	Ni	Si	Mn	P	S	Other
71.61 ± 2.13	18.41 ± 0.55	7.63 ± 0.24	1.26 ± 0.26	0.66 ± 0.11	0.03 ± 0.01	0.02 ± 0.01	0.38

The specimen with the dimension 100 mm x 30 mm x 2 mm (length l_{spec} x height h x thickness t) was vertically aligned (see Fig. 2) using a suitable clamping device. The specimens were laser cut with a machining allowance in height and then milled to the final dimension of 30 mm in height. Welding was performed along the top side with a weld seam length of length l_w of 50 mm. The weld position was aligned centrally on the top side regarding specimen thickness and length. The sheet thickness t of 2 mm (see Fig. 2) is suitable for reaching a sufficient contrast during high-speed synchrotron radiation imaging between bulk material and the keyhole and was determined in previous experiments [39].

2.2. Laser welding setup

The complete laser welding setup is depicted in Fig. 2. A disk laser (Trumpf TruDisk 8001) with a wavelength of 1,030 nm in combination with a stationary welding optics (Precitec YW52) was used for the welding experiments (see Table 2). The resulting area of interaction between laser and material is characterized from the spot size with a diameter of 0.268 mm and a focal length of the focus of 400 mm. The laser power for this laser source was selected in order to achieve a keyhole depth of approx. 1.3 mm. The keyhole depth was determined experimentally taking in consideration the visualization capabilities and ensuring to capture the entire keyhole and at the same time the melt pool on the top side using the synchrotron radiation imaging with an image dimension of approx. 2.3 mm in z-direction. The laser power was increased in steps of 100 W until the desired keyhole depth was reached, while the welding speed was set on 12 m/min in order to surely address the “single wave regime”, allowing the effect of a superimposed intensity to be investigated [7]. The sufficient size of this increment of 100 W was determined in previous investigations. The resulting laser power was 2,200 W for a welding speed of 12 m/min.

A diode laser (Laserline LDM 3000) with a wavelength of 980 nm was used as superimposed intensity to influence the welding process. A comparison of the superimposed and the disk laser intensity is shown in Fig. 3. For this purpose, the intensity of each laser beam was standardized to its respective maximum for comparison, as the intensity profile of the disk laser was measured at a lower power than that used in the welding experiments in order to protect the measurement equipment. The welding optics of the diode laser with a focal length of the focus of 100 mm was aligned at an angle of 45° under a leading configuration (see Fig. 2 and Table 2). Previous studies in [41] demonstrated that a trailing configuration leads to comparatively increased spatter formation than a leading configuration. As the aim of the superimposed intensity is to reduce spatter formation, the leading configuration was chosen for the experiments. This resulted in an elliptical spot geometry with the dimensions 1.25 mm x 1.8 mm. This size was calculated from the measured spot size with a diameter of 1.25 mm at an angle of incidence of 0°. The laser power of the diode laser was varied between 500 W, 1,000 W, 1,500 W and 2,000 W according to preliminary welding experiments. The selected powers enlarge the melt pool on the top side and reduce spatter formation. A further increase in laser power resulted in a melting of the specimen edges and was not investigated. The preliminary experiments showed no significant influence of the diode laser on the resulting welding depth. Therefore, the power of the disk laser was not adjusted and was kept constant at 2,200 W.

2.3. High-speed synchrotron radiation imaging

The welding experiments were performed at the high energy materials science (HEMS) beamline P07 (Experimental Hutch 4) of the

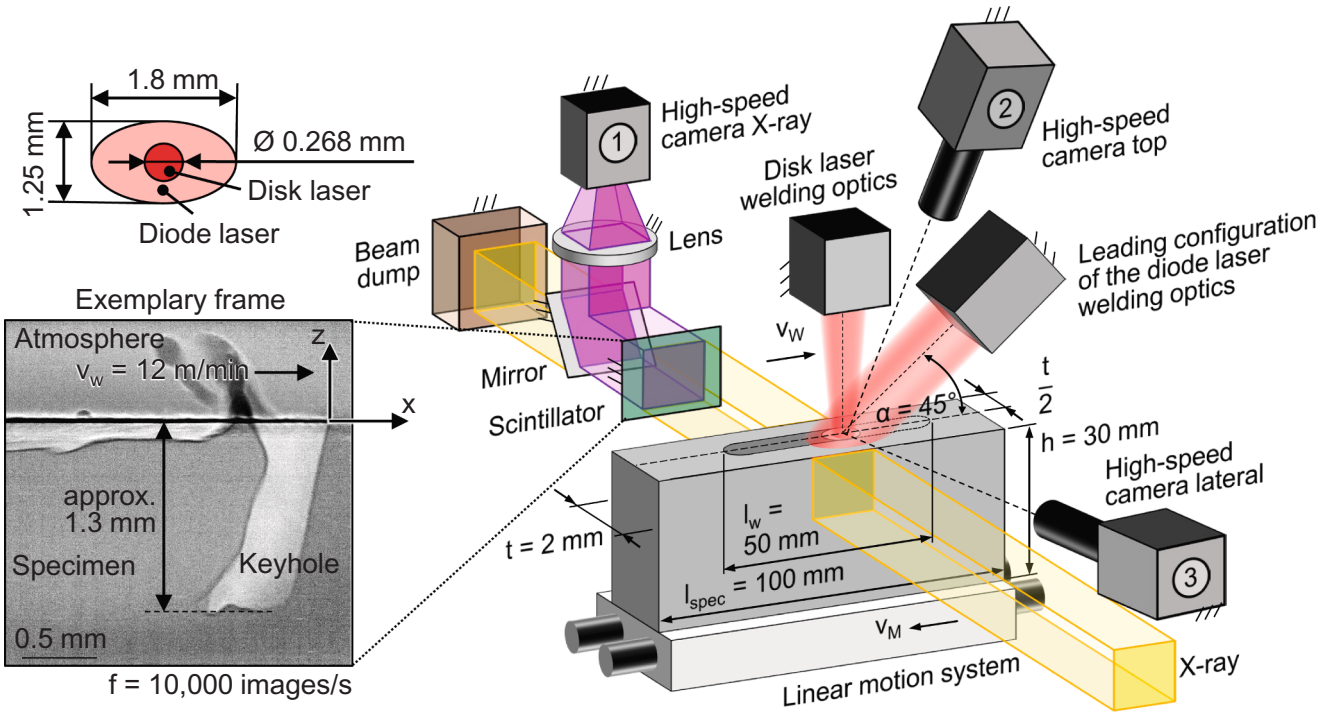


Fig. 2. Schematic illustration of the high-speed synchrotron-radiation imaging.

Table 2
Parameters of the laser welding setup (*A scanning diagnostic (Primes Focus-Monitor) system was used for measurement according to second-order-moments [40]; angle of incidence was 0°; laser powers for measurements – TruDisk 8001: 500 W, LDM 3000: 2,000 W; **Calculated values of the measured values).

Parameter	TruDisk 8001	LDM 3000
Wavelength	1,030 nm	980 nm
Max. power P_{max}	8,000 W	3,000 W
Used laser powers	2,200 W	500; 1,000; 1,500; 2,000 W
Fiber diameter	100 µm	1,000 µm
Focal length collimation	150 mm	80 mm
Focal length focus	400 mm	100 mm
Focal position z_0	Specimen surface	Specimen surface
Angle of incidence for welding α	0°	45°
Spot size for welding d	Ø 268 µm*	1.25 mm* x 1.8 mm**

synchrotron radiation source PETRA III located at the Deutsches Elektronen-Synchrotron DESY. The photon energy was set to 74 keV and the synchrotron radiation beam was converted into visible light using a Cer-doped Gadolinium Aluminum Gallium Garnet (GaGG.Ce) scintillator with a thickness of 1.2 mm. The scintillator was positioned 3.5 m behind the sample. As a result, the keyhole is visualized brighter in the images than the base material due the lower density of the metal vapor in it.

A high-speed camera (i-Speed 727, iX Cameras Ltd.) was used to record the processing zone (see Fig. 2, camera 1). The images were captured at a frame rate f of 10,000 images/s and a resolution of 1600 pixel x 900 pixel (width x height). With a scale of 2.55 µm/pixel, the recorded area has a size of 4.080 mm x 2.295 mm. The height of the area above the top side was set to 0.6 mm to record the keyhole geometry with a depth of 1.3 mm and also the spatter formation on the specimen top side. Additional information regarding the experimental setup is provided in [41].

2.4. Processing of high-speed synchrotron radiation images

The high-speed synchrotron radiation images were preprocessed for evaluation and visualization using the open source software ImageJ 2.14 [42] (see Fig. 4).

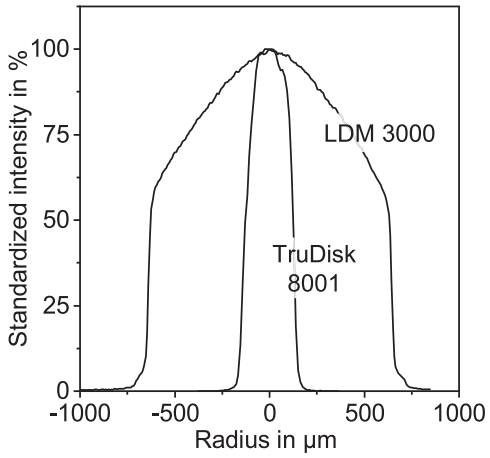


Fig. 3. Measured intensity profiles for TruDisk 8001 and LDM 3000 near the focal position along the x-axis and an angle of incidence of 0° (Laser powers for measurements – TruDisk 8001: 500 W, LDM 3000: 2,000 W; distance of the measuring position to the focal position – TruDisk 8001: 0.22 mm, LDM 3000: 0.27 mm).

A reference image was compiled by averaging 50 frames with specimen before the welding process began. In the next step, each raw image was divided by the reference to perform a flat-field correction [43]. This resulted in a corrected image with uniform brightness within atmosphere and specimen. Subsequently, brightness and contrast were adapted using the automatic adjustment of ImageJ 2.14, which applies intelligent thresholding based on the image histogram, to enhance image quality and improve the visibility of the keyhole.

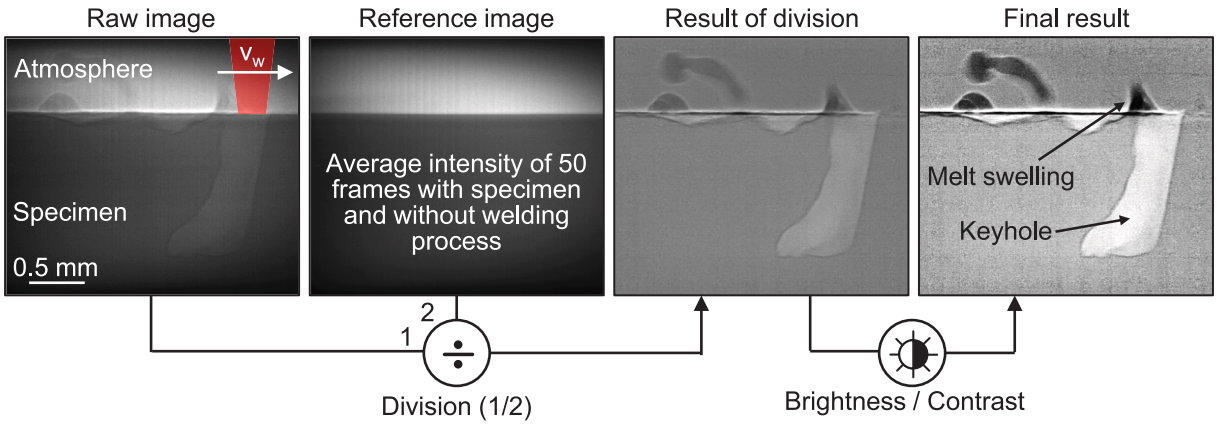


Fig. 4. Image processing for evaluation and visualization.

2.5. Highspeed videography of the top side and lateral view

To observe the keyhole and melt pool behavior on the top side, a high-speed camera (OS8, Integrated Design Tools, Inc.) equipped with a zoom lens (12x ZoomLens, Navitar, Inc.) was used at an inclination angle of 70° to the horizontal (see Fig. 2, camera 2). The top side was filmed with a frame rate of 8,000 images/s. The camera recorded an area of 13.68 mm x 9.85 mm (width x height) with a scale of 11.4 µm/pixel and an image resolution of 1200 pixel x 864 pixel. Three red LED-based light sources in different positions illuminated the specimen top side during the welding process. Therefore, a bandpass filter for the central wavelength (CWL) of 625 nm and a full width at half maximum (FWHM) of 40 nm was used to achieve a suitable brightness of the high-speed recordings.

A similar setup with a high-speed camera and a zoom lens was used to film the spatter formation from a lateral view with a frame rate of 8,000 images/s. The high-speed camera was aligned directly above the synchrotron radiation beam at an angle of 15° to the horizontal (see Fig. 2, camera 3). No additional illumination was used for the experiments. A bandpass filter for the CWL of 809 nm and a FWHM of 10 nm enabled the recording of spatter based on thermal radiation. Using an image resolution of 1600 pixel x 1200 pixel (width x height) and a scale of 15.4 µm/pixel resulted in a recorded area of 24.64 mm x 18.48 mm. This image size enabled an automatic spatter analysis of number, size and detachment angle as already described in [7]. The analysis was carried out for a 40 mm section of the 50 mm weld seam taken from the mid-length of the weld seam. This ensured that the evaluation was conducted exclusively in the steady-state of the welding process.

2.6. Tracer particles

In order to determine melt flow conditions during the welding process, tracer particles of tungsten carbide were used. Previous studies on the velocity of particles highlight that measured velocities are nearly independent of particle density and size. Appreciable differences appear only in the accelerations [44]. Likewise, in laser beam welding using X-ray imaging, investigations varying the particle size resulted in similar measured velocities [33]. Accordingly, the particles are well suited to visualize the melt flows. However, it must be noted that the used setup provides only a two-dimensional projection of a three-dimensional melt flow, which is discussed in detail below.

In a first step, the particles were classified in terms of size and geometry. An image of the particles was acquired using a reflected-light microscope and analyzed with ImageJ 2.14 (see Fig. 5). First, the automatic threshold function of ImageJ was used to binarize the image. Second, the morphological operators Erosion and Dilation removed incorrect pixels within the particles [45]. Lastly, the particle geometries were determined using the integrated particle analysis and the values for

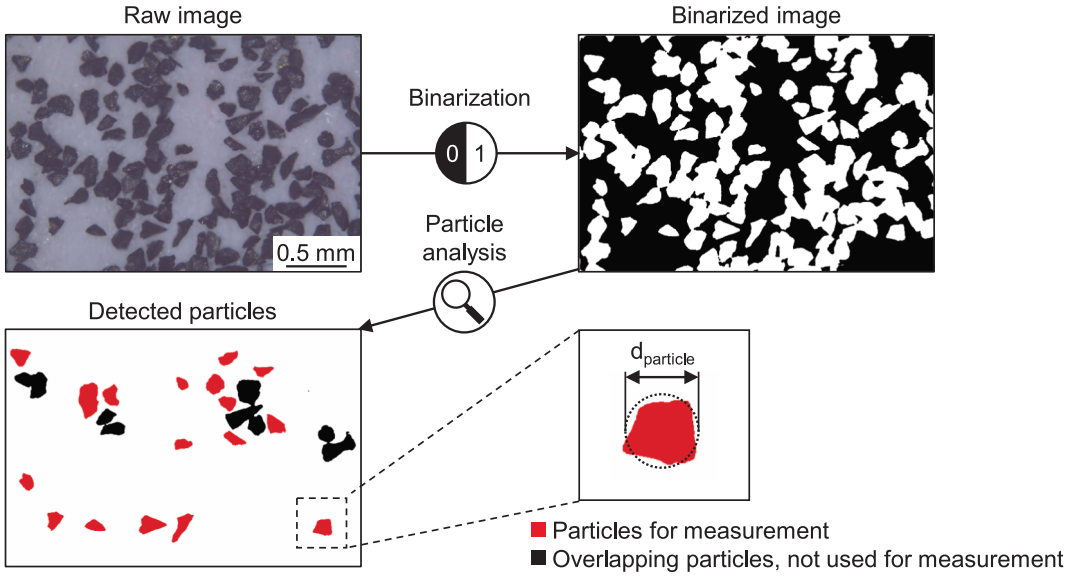


Fig. 5. Particle analysis and measurement using ImageJ 2.14.

the projected surface area and perimeter were output [46]. A total of 17 particles were used for the following analysis. Circle diameters $d_{particle}$ were calculated from the determined projected area of the microscope image to estimate and compare the particle sizes. Also, the circularity of the particles was calculated (circle perimeter divided by the perimeter of the projected particle).

As result, the particles have an average diameter of 123.66 µm ± 24.03 µm. The average circularity was 0.83 ± 0.05, where a circularity of 1 equals a perfect circle in the 2D image. The particles were placed directly on the specimen top side and in small grooves. The grooves were made manually using a center punch with an angle of 120°, resulting in a depth of the grooves of approx. 0.3 mm and a width at the top of approx. 1 mm. The particles were dragged into the melt pool during the welding process due to the melt flow. Following the clamping of the specimen into the setup, the particles were manually placed using a spatula. The particles on the top side were positioned in front, behind and into the grooves at 12.5 mm, 25 mm and 37.5 mm from the beginning of the weld seam (see Fig. 6). One welding experiment with particles and two experiments without particles were conducted for each investigated parameter setting. In this publication, only the particles directly at the top side before and after the grooves are analyzed. Specifically, these particles move along the melt pool top side, enabling insights into the melt flow around the keyhole. Particles placed in the grooves are entrained deeper into the melt pool, making them suitable for analyzing the flows behind the keyhole. Nevertheless, regarding spatter formation and its reduction, the flow near the top side, and therefore particles directly from it, are of particular relevance and will be discussed in the following.

In general, it should be noted that the particle placement can influence the welding process. For instance, a too high number of particles on the top side can reduce the energy input into the specimen. Also, the grooves can affect the melt flows due to a changed keyhole geometry during the welding process. Therefore, when selecting a particle for tracking, a certain distance to its placement and the absence of any obvious process alteration must be ensured. This distance depends on the number of particles placed and is therefore defined individually, as manual placement of the particles results in variations in their distribution.

2.7. Other

Three cross-sections were taken for metallographic examination of the resulting weld. The cross-sections were wire cut at 12.5 mm, 25 mm and 37.5 mm from the beginning of the weld seam for one specimen without particles, which means the weld can be examined during a quasi-steady behavior of the welding process. Secondary, the weld seam widths were measured at the top side for all three cross-sections.

The loss of mass was quantified using a high precision weighing device (Kern PLJ 2000-3A) with a reading accuracy amount of 0.001 g and a reproducibility of ± 0.002 g. The weight of the specimen was measured before and after the welding process. In the experiments using tracer particles, the weighing before the welding process was done without particles. After the welding process no particles remained on the specimen due to the high process dynamics. The difference between the two determined weights represents the loss of mass due to the spatter formation. Finally, the loss of mass was divided by the weld seam length. Also, a possible effect of the particles on the resulting loss of mass is examined in the following.

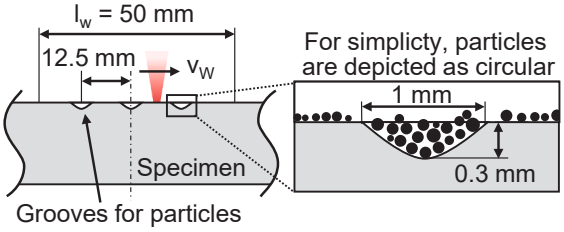


Fig. 6. Schematic illustration of particle placement.

3. Results

3.1. Reduction of spatter formation using a superimposed intensity

As described, the superposition of lasers is realized by the combination of a disk and a diode laser, each serving different functions. In order to firstly get information and insight on the superposition, three cross-sections of one specimen are analyzed. One exemplary cross-section of the specimen center (at 25 mm weld seam length) for each welding parameter is shown in Fig. 7. Furthermore, the numbers in brackets in the following are the average weld seam depths of the three cross-section.

Undercuts resulting from spatter formation are typical for the reference process without superposition, as described by [6]. With applying the diode laser the width of the solidified melt pool increases and even a low diode laser power of 500 W is already sufficient to reach first positive results regarding avoiding undercuts and reducing spatter formation, which aligns with the results of [31].

A diode laser power of 1,000 W enlarges the melt pool on the top side and thus the cross-sections in the upper part by a factor of 1.7 (from 0.49 ± 0.004 mm to 0.82 ± 0.077 mm) compared to welding without diode laser. A further increase in diode laser power to 1,500 W and subsequently to 2,000 W notably widens the weld seam. Specifically, the width of the melt pool increases also in depth, not remaining limited to the upper sheet boundary. Furthermore, molten material is visible on the top of the material on the right side for 2,000 W and will be discussed in Section 3.3. Analysis of the resulting penetration depths reveals that they are slightly larger than the keyhole depths, attributed to melt below the keyhole ground. In general, a slight increase in penetration depth was observed due to a higher energy input, comparing welding without diode laser (1.38 ± 0.02 mm) to welding with a power of 1,000 W (1.52 ± 0.01 mm). Increasing the power to 2,000 W results in a slight decrease in penetration depth (1.44 ± 0.01 mm) and will be discussed in Section 3.3. In general, at a constant power of the disk laser, the superimposed intensity of the diode laser has only a minor effect on the penetration depth.

The loss of mass Δm due to spatter formation, which was quantified by the weight change of the specimen, is presented in Fig. 8.a. Previous studies have already shown the changed weight to be a suitable parameter for describing spatter formation [7]. A relevant loss of mass due to the escaping metal vapor compared to spatter formation can be neglected. An approximate calculation of the loss of mass due metal vapor using experimentally determined values for a comparable setup in [47] results in a loss less than 0.05 mg/mm. In order to have a preliminary insight in the relevance and effects of tracer particles under the restrictions at DESY, a comparative study was performed and the results are summarized in Fig. 8.a. While out of three repetitions two were carried out without, the third was carried out with particles. The complexity of the setup and the limited experimental time at DESY did not allow a higher number of verification experiments. Nevertheless, the different experiments confirm the consistency of the results. A relevant influence of the tracer particles to the welding process is not significant because of low deviations in loss of mass over all the experiments. Only slightly lower values were identified that are attributed to particles trapped in the melt pool. Using the mean particle diameter of 123.66 µm and a tungsten carbide density of 15,600 kg/m^3 [34], a mean particle mass of approx. 16 µg is obtained. Therefore, a measured mass difference $\Delta m = 0.1$ mg would correspond to six to seven particles per millimeter of the weld seam length. This equates to 323 tracer particles for a weld seam length of 50 mm.

The diode laser at a power of 500 W results in a slight reduction in

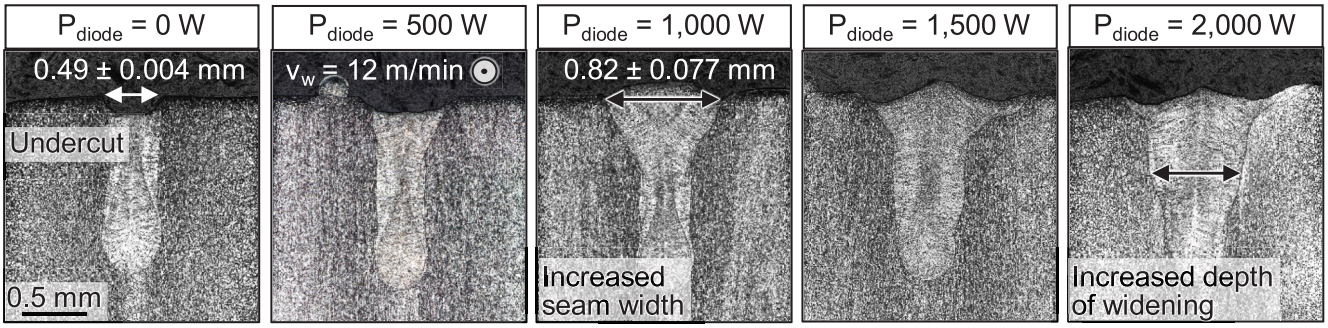


Fig. 7. Cross-sections of the specimen center (25 mm) for a welding speed of 12 m/min and different diode laser powers.

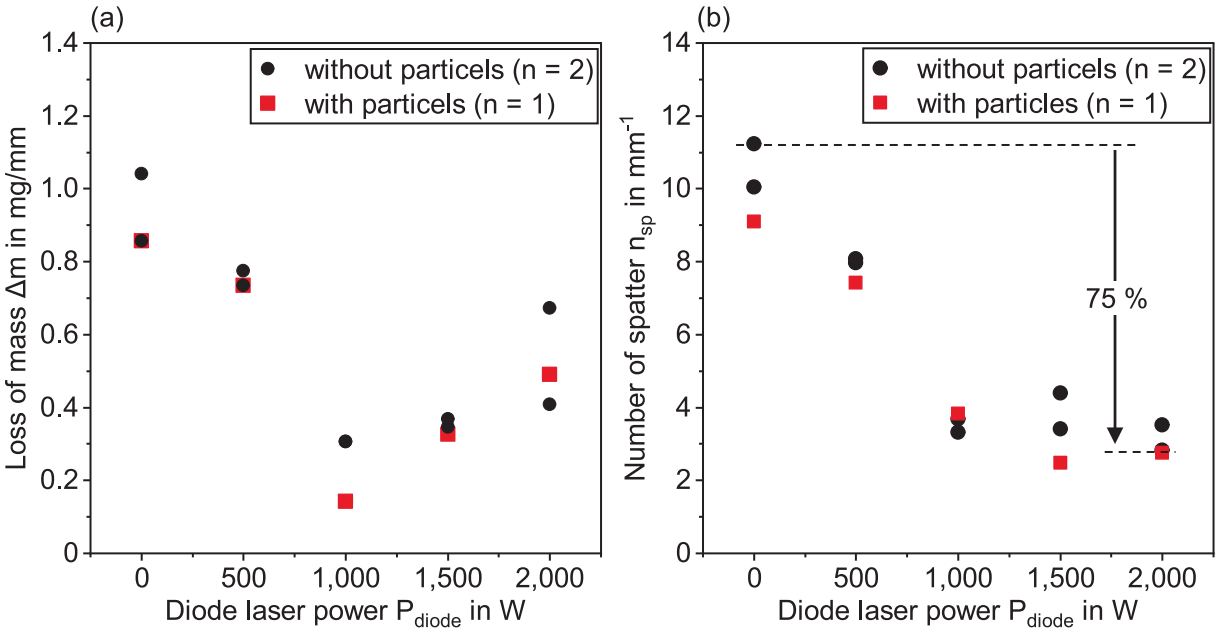


Fig. 8. Quantification of the spatter formation for a welding speed of 12 m/min and different diode laser powers; (a) Loss of mass of one specimen, (b) Number of spatter for 40 mm weld seam.

loss of mass. Switching to a diode laser power of 1,000 W reduces the loss of mass in all experiments to below 0.4 mg/mm. A further increase to 1,500 W has only a minor additional effect. However, the loss of mass increases again when the diode laser power is raised to 2,000 W. The cause of the initially reduced and subsequently slightly increased loss of mass is described in detail below.

The lateral high-speed recordings were analyzed to quantify the number of spatter n_{sp}, which represents the number of spatter per millimeter of weld seam. To further investigate the correlation between loss of mass and the number of spatter, the measured values were compared (see Fig. 8.b). The number of spatter correlates to the loss of mass and similarly decreases with increasing diode laser power up to 1,000 W. Higher laser powers of 1,500 W and 2,000 W result in comparable amounts of spatter. Therefore, the increase in the loss of mass can be attributed to a larger spatter size and is discussed below.

An increase in spatter adhesion on the top side does not occur and can be excluded due to the narrow specimen geometry of 2 mm. In summary, the number of spatter is reduced by up to 75% in case of a superimposed intensity with a diode laser power $>$ 1,000 W.

The stack images in Fig. 9.a, b and c provide an initial overview of the process behavior and spatter formation, complementing the previous quantification of spatter formation based on loss of mass and number of spatter. They represent the identical time span with a specific number of images n = 200 and a specific time interval $\Delta t = 1$ ms between them. This correspond to a defined time window of the welding process and represent 40 mm of the welding length in the center of the weld seam. The images were generated using the maximum intensity projection (MIP), a method that visualizes the highest pixel values in each dataset. The settings of 0 W, 1,000 W and 2,000 W are chosen respectively following the results in Fig. 8.a, where applying 1,000 W leads to the lowest loss of mass and increasing to 2,000 W leads to an increase.

Welding without the superimposed diode laser results in spatter formation opposite to the welding direction within an angle of approx. 50°, as presented by the red arrows and the red dashed line in Fig. 9.a. This is also apparent in Fig. 9.d, where the spatter detachment angle α_{sp} is plotted versus the spatter size for the same welded length of 40 mm. Furthermore, smaller spatter generally detach at larger angles relative to the specimen top side. The spatter size is given by the projected area A_{sp} recorded in the high-speed images. It was determined by an algorithm that averages the multiple projected spatter areas along one spatter trajectory. Assuming a spherical spatter, the diameter d_{sp} can be calculated from the projected area. No spatter smaller than approx. 0.015 mm^2 were detected due to the limited image resolution in combination with a reduced incandescence as spatter size decreases. This must be considered during the evaluation but does not affect the overall

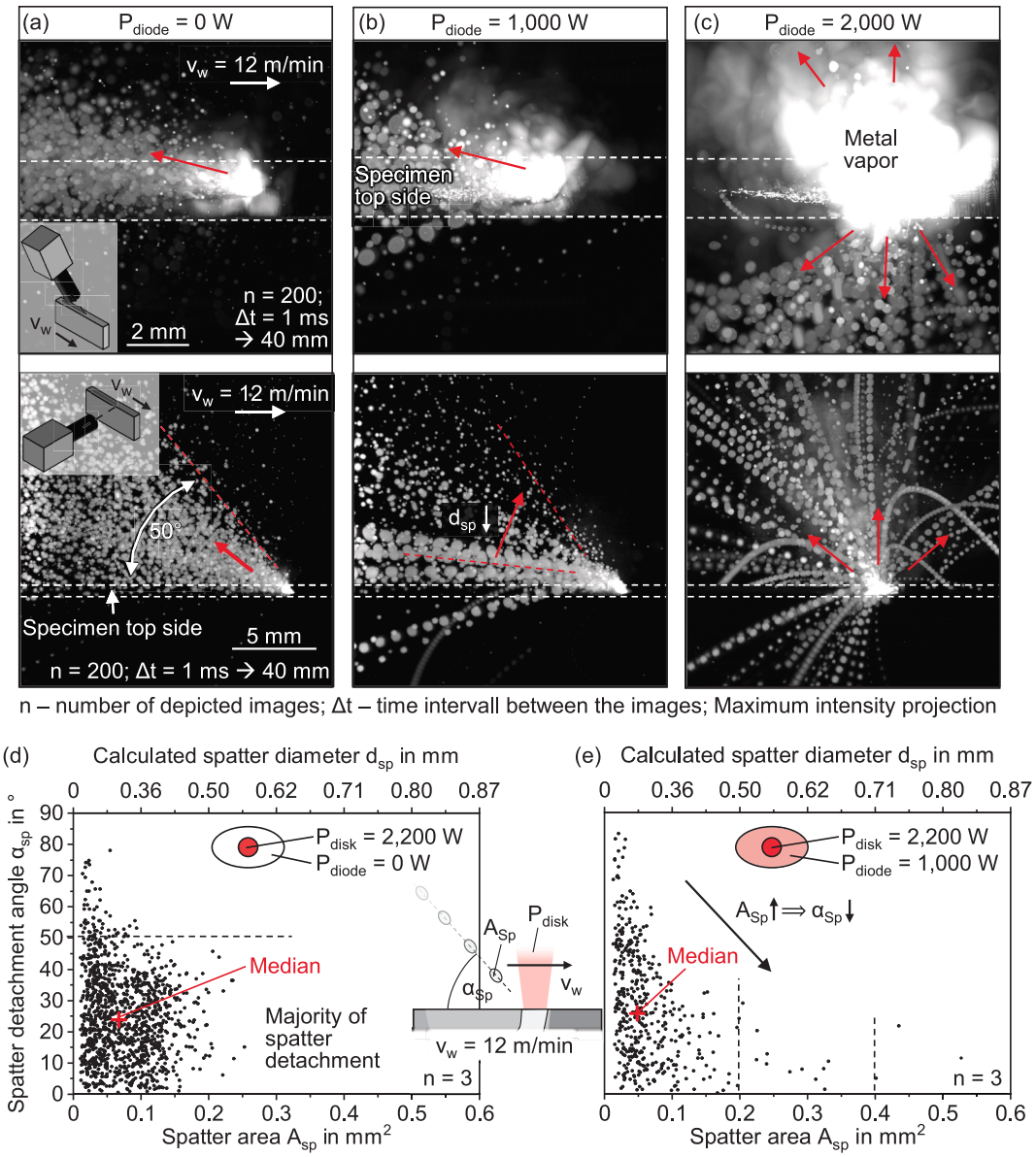


Fig. 9. Stack images of the specimen top side and of the lateral high-speed recordings for a welding speed of 12 m/min; (a) Process without diode laser, (b) Diode laser power of 1,000 W, (c) Diode laser power of 2,000 W; and correlation between spatter size and detachment angle; (d) Process without diode laser, (e) Diode laser power of 1,000 W.

description.

The spatter trajectories are also directed opposite to the welding direction using the diode laser with a power of 1,000 W (see Fig. 9.b). The number of spatter and therefore spatter formation can be significantly suppressed and in particular the distribution of spatter size is larger, as single spatter with a projected area over 0.4 mm^2 can be detected (see Fig. 9.e). In contrast, the median value decreases slightly from 0.067 $mm^2 \pm 0.035$ mm^2 to 0.048 $mm^2 \pm 0.021$ mm^2. In the region below 0.4 mm^2 the highest number of spatter is of 0.05 mm^2 up to 0.10 mm^2. The individual spatter with a high projected area over 0.2 mm^2 detach with a small angle, which can be much lower than 25°. In particular, comparatively large melt swellings lead to large spatter. As a result, the droplet remains connected to the melt swelling for a longer time due to the effect of surface tension [48]. The trajectory of the spatter is deflected parallel to the surface by the reabsorption of the melt swelling into the melt pool [49]. If the flow velocity is further reduced, the droplet does not detach from the melt swelling, and no spatter forms. A calculation of the loss of mass based on the spatter areas of all detached spatter, assuming a spherical shape, shows a reduction of 70% when using the diode laser. This is consistent with the measured loss of mass and the number of spatter described above.

Increasing the power of the diode laser to 2,000 W results in an altered spatter formation (see Fig. 9.c). Spatter detach undirected and therefore cannot be analyzed with respect to the detachment angle using the algorithm described above. However, the spatter area can still be determined and increases to 0.075 $mm^2 \pm 0.044$ mm^2. Some of the spatter have a curved trajectory due to their low kinetic energy $E_{kin,sp}$, which results in a reduced spatter velocity. The reduced kinetic energy is attributed to occasional lateral spatter detachment that occurs at higher diode laser power out of the enlarged melt pool, details are provided in Section 3.3. The trajectories are influenced by the gravitational force, depending on spatter size and velocity [50]. Furthermore, it can be observed that the diode laser power leads to higher temperatures and high brightness in the interaction area. These facts are also confirming the results of Fig. 7 and the changing geometry of the keyhole. Moreover, the flow of the metal vapor is influenced using the diode laser

power 2,000 W, detectable on the white area directly above the keyhole for the top side view in the upper part of Fig. 9.c. It is assumed, that the additional energy widens the keyhole at the top side and leads to an increased amount of evaporated material. A detailed description of this phenomenon is provided in the following.

3.2. Keyhole and melt pool behavior without diode laser

The following section presents a detailed analysis of melt pool and keyhole behavior in order to examine the effects described above. Fig. 10 depicts four consecutive frames of the high-speed recordings from the top side and the synchrotron radiation recordings in Fig. 11 show the time-dependent process behavior of the spatter formation primarily from a region behind the keyhole rear wall.

The images do not allow to clearly observe the melt flow in front and lateral of the keyhole (see Fig. 10). This is depending on overexposure effects and a thin extension of the melt pool compared to the keyhole. Nevertheless, the formation of a melt swelling and a melt column can be detected. Furthermore, the fluctuation of the keyhole can be indicated due to the behavior of the metal vapor flow, which changes in the four different time steps. During the first frame (t_0) the vapor plume is oriented upward, while after 0.125 ms the vapor flow is opposite to the welding direction according to melt swelling direction.

Fig. 11 gives a clearer insight in spatter detachment of an exemplary image sequence recorded by synchrotron radiation imaging. A melt swelling emerges behind the keyhole aperture (t_0 + 0.2 ms) and develops into a melt column (t_0 + 0.4 ms). During this process, a melt pool depression can be observed behind the melt swelling. A spatter detaches by necking the melt column (t_0 + 0.6 ms). Contemporary to the development of the melt swelling to a melt column and a spatter, the keyhole changes its shape as well. The extension of the bulging phenomena at the ground of the keyhole and the behavior of the keyhole rear wall give a complementary information on the fluctuation frequency of the keyhole. In contrast to this observation it has to be stated that the keyhole front does not fluctuate [51].

3.3. Increasing the melt pool and reducing spatter formation

Applying the diode laser with a power of 1,000 W affects the keyhole and melt pool behavior and thus leads to a spatter reducing effect through superimposed intensity.

The diode laser interaction leads to an increase of the melt pool size on the specimen top side (see Fig. 12). The keyhole is surrounded by a large melt pool at the front and outside. Due to the enlarged melt pool and the reduced spatter formation, this process behavior is referred to as “Enlarged melt pool and reduced spatter formation”. Despite the overall reduction in spatter formation, the chosen image series shows a spatter detachment by the formation of a melt swelling and subsequent a melt column (t_0 + 0.25 ms), similar to welding without the diode laser. A single spatter is visible at t_0 + 0.50 ms and t_0 + 0.75 ms.

However, the melt swellings or melt columns frequently fall back into the melt pool without any spatter detachment in contrast to the previous experiments without the superimposed diode laser. This behavior was repeatedly observed in the recordings and is shown as an example in Fig. 13 (t_0 + 0.5 ms). Subsequently, the melt swelling is reabsorbed by the melt pool (t_0 + 1.5 ms), which results in a reduced spatter formation. The condition in the melt flow leading to this behavior and especially the melt flow velocity v_{fl} are studied in detail in order to verify the assumption of a lower melt velocity.

The keyhole geometry with a stable front and a fluctuating rear wall is comparable to welding without the diode laser. Only a slight effect on keyhole behavior and geometry was observed during the evaluation of the synchrotron radiation images in 50 subsequent frames. At a depth of 0.1 mm from the top side the keyhole length l_t seems to be slightly reduced when a diode laser power of 1,000 W is applied (see Fig. 14.a). This effect is attributed to the enlarged melt swelling behind the keyhole aperture due to the reduced spatter formation. The hydrostatic pressure of this melt causes a slight reduction in keyhole length. The described effect only occurs on the top side while no considerable change in length is observed in the keyhole center l_c (see Fig. 14.b). In addition, bulging at the keyhole bottom is diminished (see Fig. 14.c). The reduction in bulging is attributed to a velocity decrease of the downwards directed melt flow at the keyhole front [52], which is deflected at the bottom. Thus, a direct correlation seems to exist between the reduced bulging at the keyhole bottom and the decreased spatter formation. However, it should be noted that both phenomena result from reduced melt flow velocities and are therefore not directly dependent on each other. A detailed analysis of the flow velocities is provided in Section 3.4.

The increase of the keyhole length near the top side by using 2,000 W of the diode laser is well detectable even in high-speed images. Indeed, the size of the melt pool is notably larger than the keyhole aperture, similar to welding with a diode laser power of 1,000 W (see Fig. 15, e.g., t_0 + 0.5 ms). An increased and fluctuating outflow of the visible metal vapor is observed as well. Melt swellings and spatter formation do not occur behind the keyhole. Furthermore, spatter detach lateral out of the melt pool (t_0 + 1.5 ms).

A melt swelling forms at the keyhole side (see Fig. 16, t0 + 0.5 ms), followed by the formation of a melt column (t_0 + 1.0 ms). A spatter detaches by necking and falls down the sheet sides. The lateral melt swelling results from the altered melt flows and increased pool size. It can be assumed, that the melt flow around the keyhole is reduced due to the larger melt pool and the resulting larger cross-section of the flow. In particular, the effect of the upwards directed melt flow on the keyhole sides due to escaping metal vapor from the keyhole front and rear wall appears to increase, which may contribute to the lateral melt swellings with subsequent spatter formation. This upwards directed melt flow on

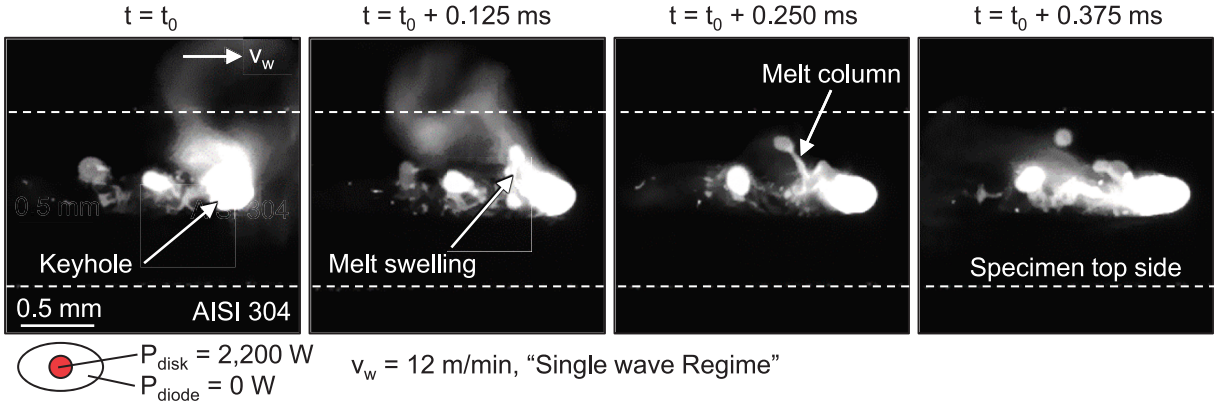


Fig. 10. Time-dependent process behavior of the top side for a welding speed of 12 m/min.

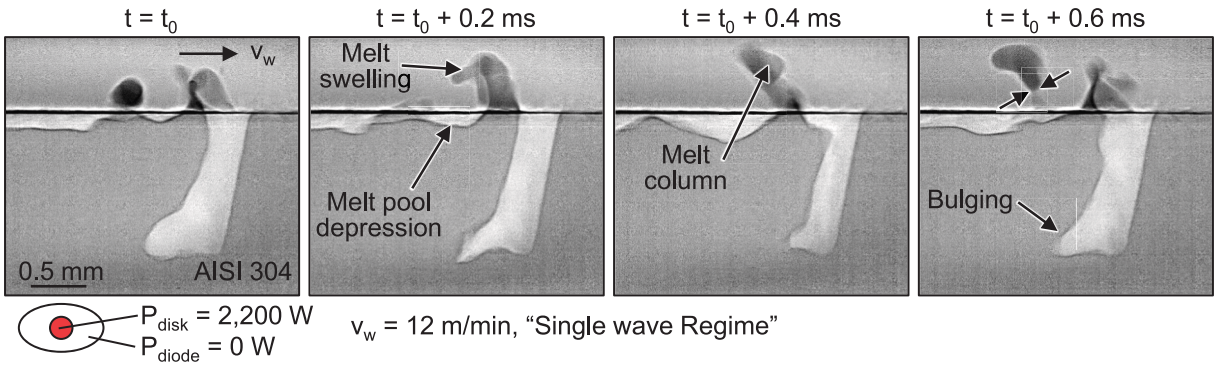


Fig. 11. Time dependent process behavior for a welding speed of 12 /min using high-speed synchrotron radiation imaging.

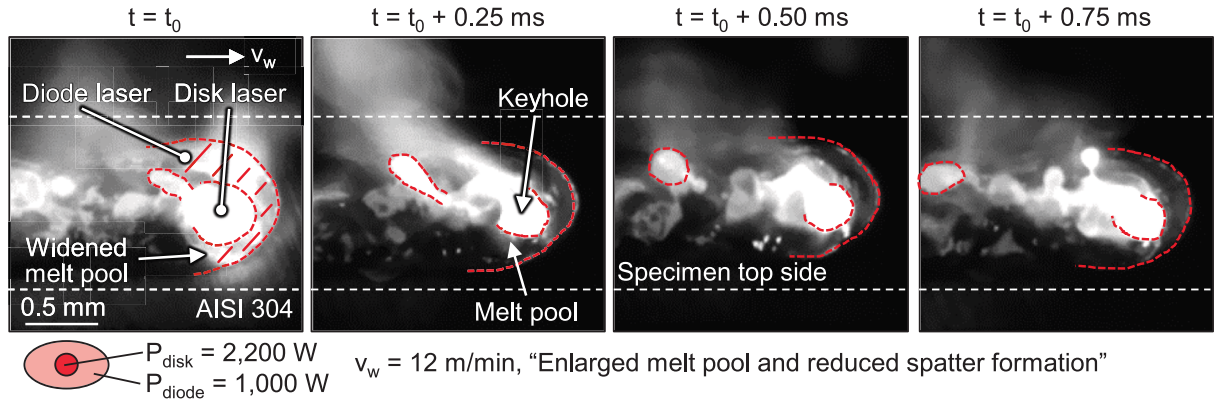


Fig. 12. Increased melt pool on the top side for a welding speed of 12 m/min and a diode laser power of 1,000 W.

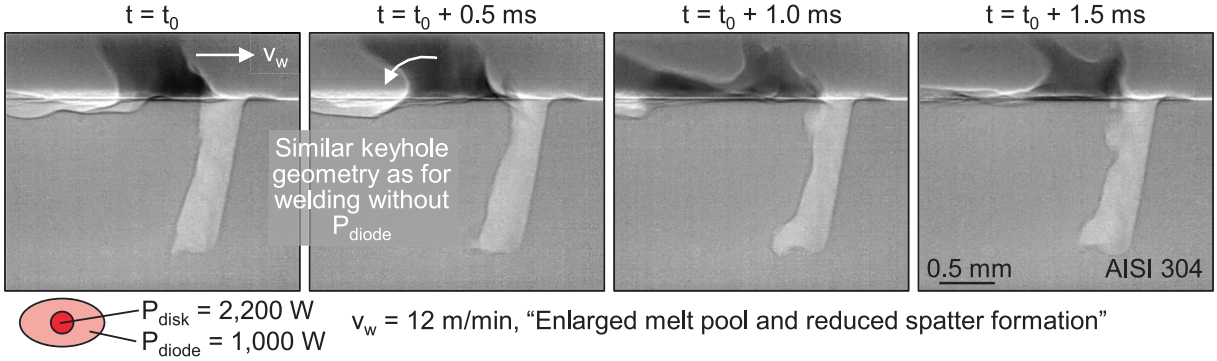


Fig. 13. Time dependent process behavior for a welding speed of 12 /min and a diode laser power of 1,000 W using high-speed synchrotron radiation imaging.

the keyhole sides can be seen by using tracer particles during synchrotron radiation imaging. Fig. 17 shows the movement of such an exemplary particle from the melt pool behind the keyhole to the top side. This behavior does not occur as a single event but represents a continuously repeating phenomenon. No comparable melt flow was observed at lower diode laser powers. Due to the elongated keyhole geometry and the lateral spatter formation, this behavior is described as "Elongated keyhole and lateral spatter formation".

Fig. 18 indicates that the diode laser beam hits directly on the keyhole rear wall with high energy enlarging the keyhole length opposite to the welding direction. The energy of the disk laser, however, forms the keyhole by evaporating material from the front (see Fig. 18). The overall keyhole elongation due to the diode laser is most pronounced at the top side and diminishes with increasing keyhole depth as described before. The maximum intensity of the diode laser in the center of the spot geometry results in the highest energy input at half of the depth of the keyhole rear wall. A keyhole bulge forms at this location on the keyhole rear wall, which fluctuates strongly, as indicated by its varying shapes in Fig. 16.

The energy input through the diode laser increases the vaporization of the material on the keyhole rear wall and therefore advantages the formation of the bulging, also resulting in the increased volume of metal vapor outflow. Bulging and melt flow behavior are related to each other in this time interval while metal vapor from the rear wall and escaping from the keyhole tends to enlarge the keyhole length l_t on the upper side. The melt flows and connected phenomena due to pressure dependency from surface tension tend to close the keyhole. The dominant flow components are the melt flow around the keyhole [13] and the flow directed downwards at the keyhole front [24] that is deflected at the keyhole bottom, as described in literature. As result, the keyhole rear wall is fluctuating (see Fig. 16). These fluctuations displace the melt pool and support the lateral spatter formation. Furthermore, the oscillation of

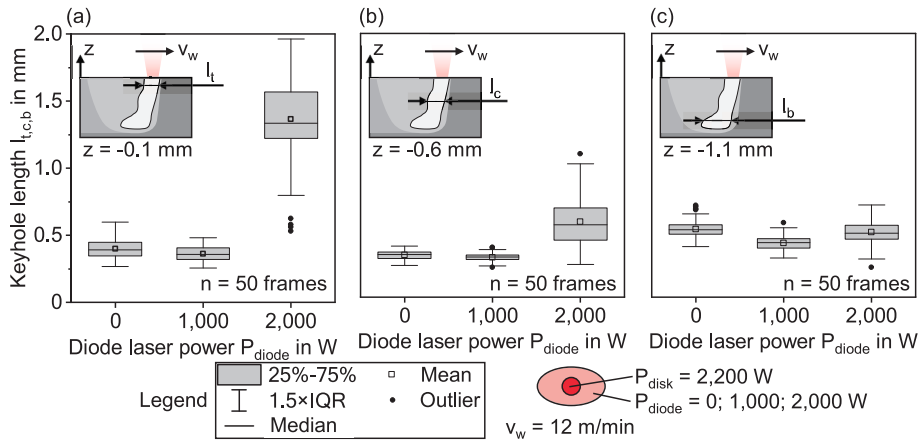


Fig. 14. Effect of the diode laser on keyhole length at different positions.

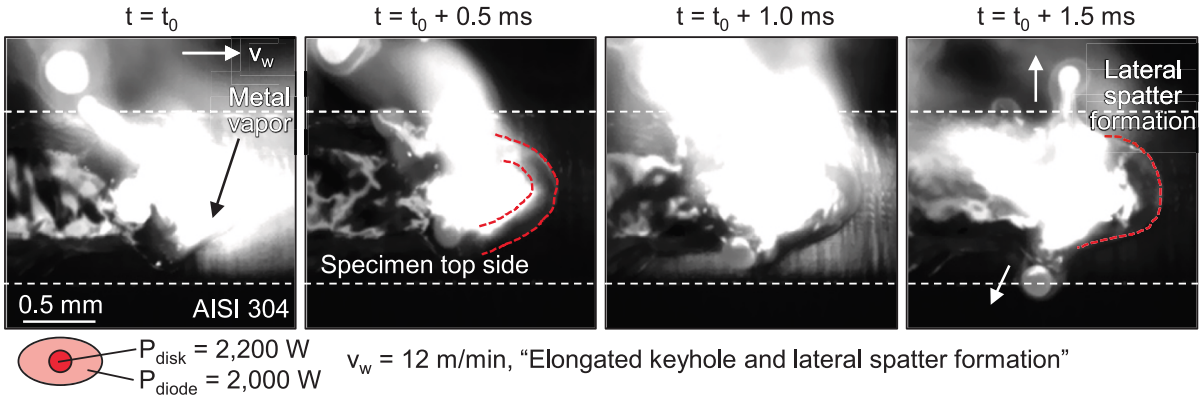


Fig. 15. Time-dependent process behavior of the top side for a welding speed of 12 m/min and a diode laser power of 2,000 W.

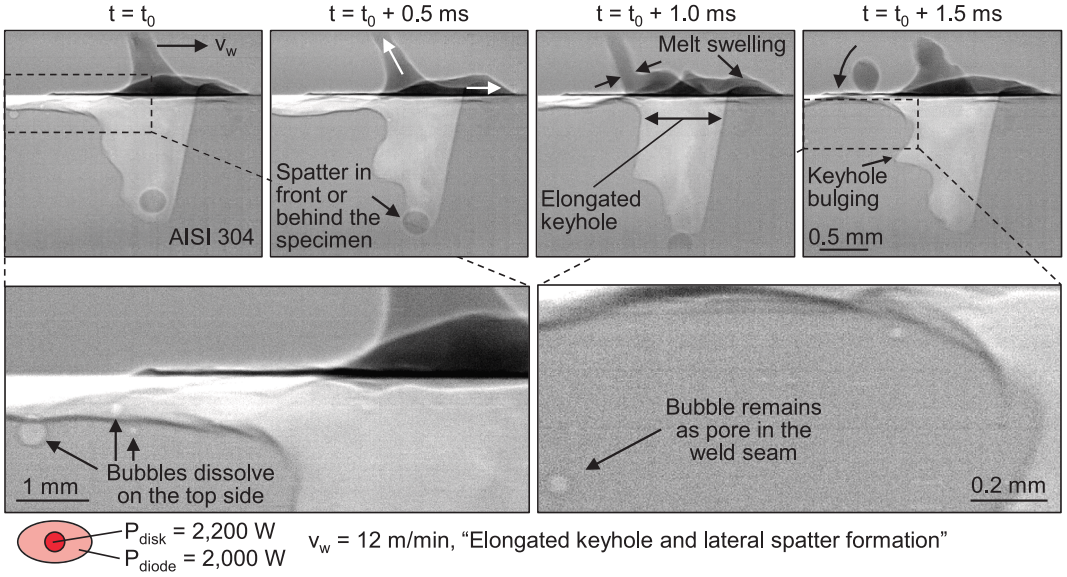


Fig. 16. Time dependent process behavior for a welding speed of 12 m/min and a diode laser power of 2,000 W using high-speed synchrotron radiation imaging.

the rear wall causes fluctuations in the metal vapor flow. As the bulging decreases, the pressure inside the keyhole increases effecting the metal vapor flow. Finally, the upward directed melt flow on the keyhole rear wall is strongly influenced or suppressed. As the upward directed melt flow no longer occurs and the keyhole aperture widens, the formation of a melt swelling behind the keyhole is suppressed. The formation of this melt swelling is directly associated with spatter formation, as the spatter detach from the swellings through necking. Consequently, spatter formation from the region behind the keyhole is no longer observed.

In addition to the lateral spatter formation, bubbles form in the upper

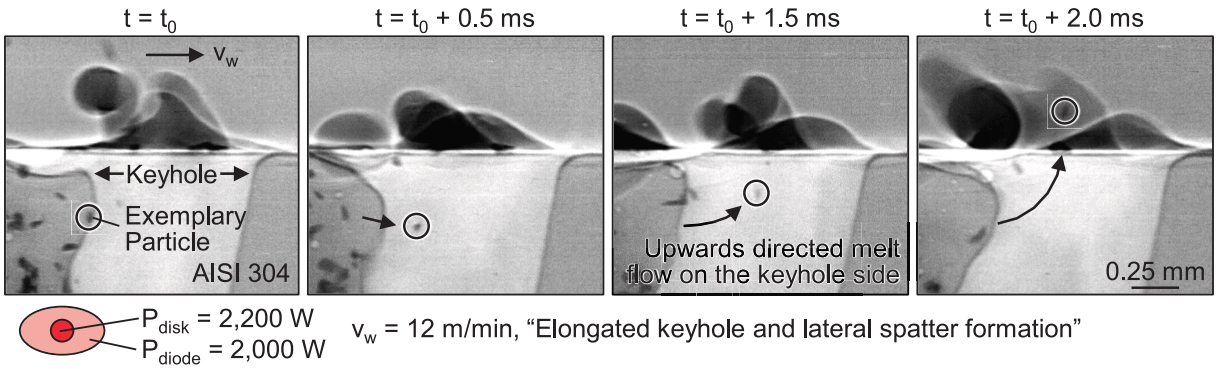


Fig. 17. Melt flow at the keyhole side causing lateral spatter formation.

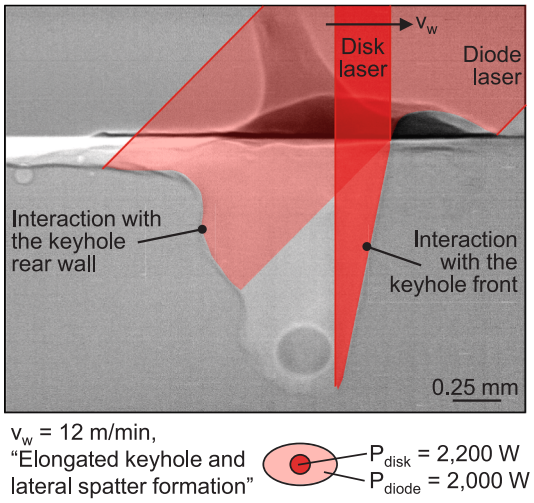


Fig. 18. Interaction regions of the disk and the diode lasers with the keyhole walls for an exemplary frame.

region of the melt pool behind the keyhole and remain sporadically as entrapped pores in the weld seam (see Fig. 16, detailed views below the image series). It can be assumed that the fluctuations of the keyhole and melt pool cause these bubbles, which occasionally trap ambient atmosphere or metal vapor within the melt pool. A part of the formed bubbles remains retained as pores in the weld seam due to the solidification process of the melt. A further part of the bubbles rises to the surface and dissolves there. Some of the bubbles also dissolve within the weld pool, indicating metal vapor recondensing inside [53].

3.4. *Experimental determination of the melt flow at the keyhole front and around the keyhole*

The trajectories of the tungsten carbide tracer particles are studied in order to determine the melt flow direction as depicted in Fig. 19. The results are described in this chapter based on the tracking of particles from the specimen top. The particles were dragged into the melt pool in front of the keyhole and tracked until they reached the keyhole rear wall, only particles exhibiting this type of motion were tracked. Particles showing different behavior are not considered in this analysis. The melt flow around the keyhole and the downward flow at the keyhole front can be analyzed through decomposition of the velocity components. The particle movement in the y-direction is neglected due to the setup.

The figure depicts the trajectories of 20 single particles in time steps of 0.1 ms comparing the effect of different diode laser powers and considering the geometry of the keyhole. When the diode laser is switched off (0 W) the particles move in the negative x- and z-direction probably around the keyhole reaching the keyhole rear wall in a range of approx. −0.5 mm (z-direction). Only one particle seams to follow the downward flow on the keyhole front wall. When the diode laser power enhances to 1,000 W, a higher concentration of particle trajectories can be resolved below −0.25 mm (z-direction) moving from the front to the rear of the keyhole. While with 2,000 W a clear bifurcation of the trajectories also due to the geometry of the keyhole can be observed. The

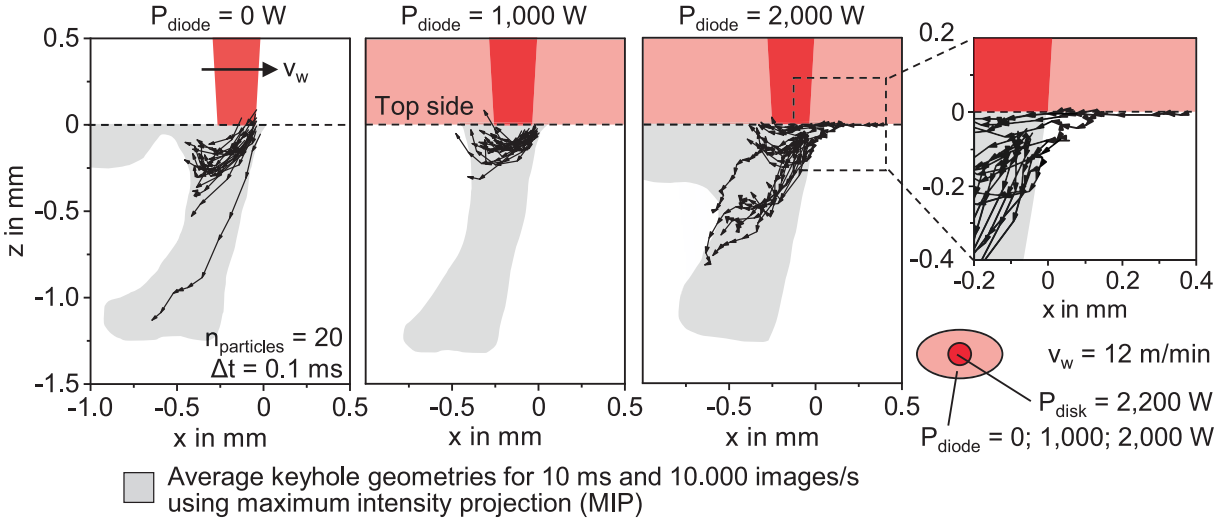


Fig. 19. Visualization of particle trajectories from the specimen top side in front of the keyhole.

velocities of the particle trajectories are determined in the following evaluation.

To determine the velocities, each particle was analyzed based on its trajectories between the time steps of 0.1 ms. In a first step, the maximum magnitude of velocity v_{fl_max} was determined, corresponding to the highest particle speed within the trajectory. In addition, the horizontal and vertical melt flow components are examined. The horizontal velocity component (x-direction) gives information on the flow around the keyhole, and the vertical component (z-direction) on the downward flow at the keyhole front. The flow opposite to the welding direction (negative x-direction) results of the circumferential flow around the keyhole (influenced by the increasing of the liquid film through the diode laser). The downward flow (negative z-direction) refers to the flow at the keyhole front (laser hitting the front wall). Therefore, one trajectory in the x- and one in the z-direction were determined for each particle, using the lowest value to obtain the highest velocities opposite to the directions defined by the coordinate system. Thus, the diagrams show the minimum velocities for both components. The following descriptions refers to the absolute values of these two velocities.

Increasing the diode laser power to 1,000 W decreases the mean and median flow velocity of 0.5 m/s for the magnitude of velocity (see Fig. 20, left). The melt flow velocity remains almost constant for a further increase of diode laser power. The absolute melt flow velocity in x-direction decreases (see Fig. 20, center), increasing the diode laser power to 1,000 W. The velocity remains almost constant for higher laser powers. Enlarging the melt pool on the sheet top side results therefore in a reduction of the horizontal velocity, which confirms the assumption. The flow cross-section increases and, consequently, the melt flow velocity reduces. The melt flow energy decreases (see Equation (1), minimizing the probability of a spatter detachment. Consequently, as described above, the number of spatter is reduced.

The diode laser with a power of up to 1,000 W increases the flow cross-section in z-direction (see Fig. 20, right) similar to the horizontal velocity component. Therefore, the velocity of the downward melt flow at the keyhole front is reduced. As discussed above, reducing the velocity of this flow component diminishes bulging at the keyhole bottom. Higher diode laser powers increase the scattering of the measured velocities. The melt pool is widened up at the top side and extends to approx. half of the welding depth for higher powers. As a result, some particles are dragged deeper into the melt pool, and the scattering of the velocities increases.

The measured values, particularly for the melt flow around the keyhole, are comparable to those reported in literature. In addition to the welding speed, these values strongly dependent on the keyhole diameter and often represent maximum values directly at the liquid–vapor interface. For instance, [26] calculates velocities of about 1 m/s for a smaller keyhole diameter of 0.2 mm, while [54] provides calculated values for different keyhole sizes and for a comparable size to the experiments of approx. 3 m/s. Simulations in [51], using a comparable setup, also reveal velocities in a range of approx. up to 3 m/s. The presented velocities here for welding without diode laser are in the range of 0.75 to 1.25 m/s with an average value of 1.0 m/s and are therefore slightly lower. However, the measured velocities are expected to be lower than the real velocities which can be explained with the fact, that due to the imaging technique a 2D-image is evaluated, while in the reality it is to be assumed that the particle moves on a curve and not a straight path. Nevertheless, this limitation is common for X-ray imaging. Assuming a circular keyhole aperture, the actual 3D-movement of the particles respectively the melt corresponds to a factor of 1.6 compared to the depicted movement in the synchrotron radiation images (see Equation (2)). This factor results from the ratio between half of the keyhole circumference, calculated using the keyhole length at the top side, and the measured traveling distance of a particle (l_t):

$$\frac{\pi}{2}\frac{l_t}{l_t}=\frac{\pi}{2}\approx 1.6. \tag{2}$$

Accordingly, a correction of the measured values would be possible and would result in values in the range of 1.2 to 2 m/s, which closely match the current state of the art.

For the downward directed melt flow at the keyhole front, [55] reports velocities in the range of 9 to 15 m/s with a dominant value of 7.5 m/s [56], which were determined by high-speed recordings of the keyhole front. Due to the narrow melt film at the keyhole front, calculated to be approx. 100 µm in thickness [56], the comparatively large particles (average diameter of 123.66 µm in this study) can only approximate this flow with noticeable deviations. In addition, only occasional particles were entrained into the depth, whereas the majority were diverted by the melt flow around the keyhole.

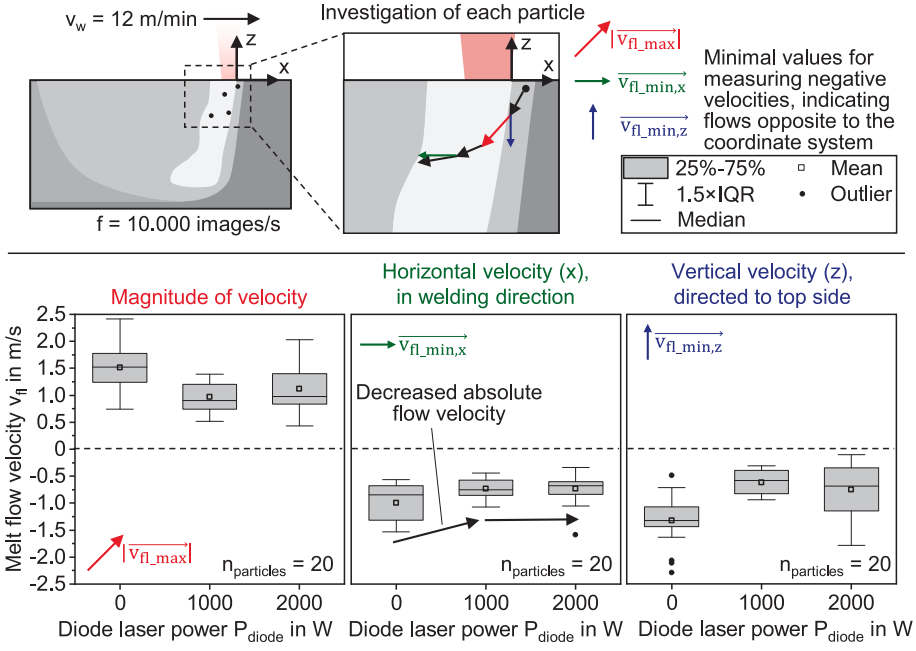


Fig. 20. Measurement of the melt flow velocities for particles from the keyhole front, a welding speed of 12 m/min and different diode laser powers.

4. Conclusion

The investigation had the scope to bring new insights in order to clarify the effects of laser beam intensity superposition on melt flow and spatter formation during laser welding of austenitic stainless steel. Phenomenologically a reduction of spatter with a second laser with lower intensity hitting on the material was stated in literature, while information on the effect on the melt flows were generally missing. Due to investigations with synchrotron radiation and tungsten carbide particles fully new insights and a deeper understanding and description are possible. Depending on the superimposed diode laser power, three scenarios can be highlighted (see Fig. 21).

The reference process without additional diode laser power corresponds to the well-known "Single wave regime" with a high number of spatter and loss of mass (see Fig. 21a). Therefore, a melt swelling behind the keyhole aperture forms and out of it a melt column. Spatter detach by necking of the melt column and the melt swelling forms again. The melt pool around the keyhole is only slightly larger than the keyhole geometry. The melt flow moves with velocities of approx. 1.2 m/s in z-direction downward at the keyhole front wall and approx. 1 m/s around the keyhole.

Using a diode laser as superimposed intensity (1,000 W) increases the melt pool on the top side (Fig. 21b). Increasing the flow cross-section reduces the mean melt flow velocity of the flow around the keyhole to approx. 0.8 m/s. Thus, the spatter formation is significantly reduced by 60%. Consequently, influencing the melt flows is particularly effective for reducing the spatter formation due to a lower kinetic energy of the melt flow. Due to the enlarged melt pool, the downward directed melt flow at the keyhole front is significantly reduced by approx. 50%.

A higher diode laser power (2,000 W) increases the depth of the enlarged melt pool at the front and the sides due to the higher energy input. The melt flow velocity of the flow around the keyhole is also reduced to 0.8 m/s for this higher power compared to the reference experiment without diode laser. A further decrease in this flow velocity relative to the previously diode laser power was not identified. The laser radiation with an angle of 45° expands the keyhole on the rear wall due to the vaporization and forms a bulging. This bulging fluctuates and therefore disturbs and almost completely suppresses the upward flow on the keyhole rear wall. However, the enlarged melt pool results in a lateral spatter formation. The escaping metal vapor from keyhole front and rear wall in combination with the fluctuation of the bulging results in an occasional melt flow at the keyhole sides and results in these spatter. The suppressed upward directed melt flow at the keyhole rear wall and the lateral spatter formation are not directly linked. Rather, both phenomenon result from the fluctuations of the keyhole rear wall and the widening of the melt pool. Furthermore, small pores form due to the trapping of metal vapor or ambient atmosphere.

In summary, if the power of the superimposed intensity is too high, the melt pool is fluctuating resulting in weld seam imperfections such as pore and spatter formation. The power of the diode laser must therefore be sufficiently high to enlarge the melt pool on the top side, but not as high to affect the keyhole behavior in the depth. This effectively reduces the velocity of the melt flow around the keyhole and thus the spatter formation.

5. Data availability

The data presented in this study are available on request from the

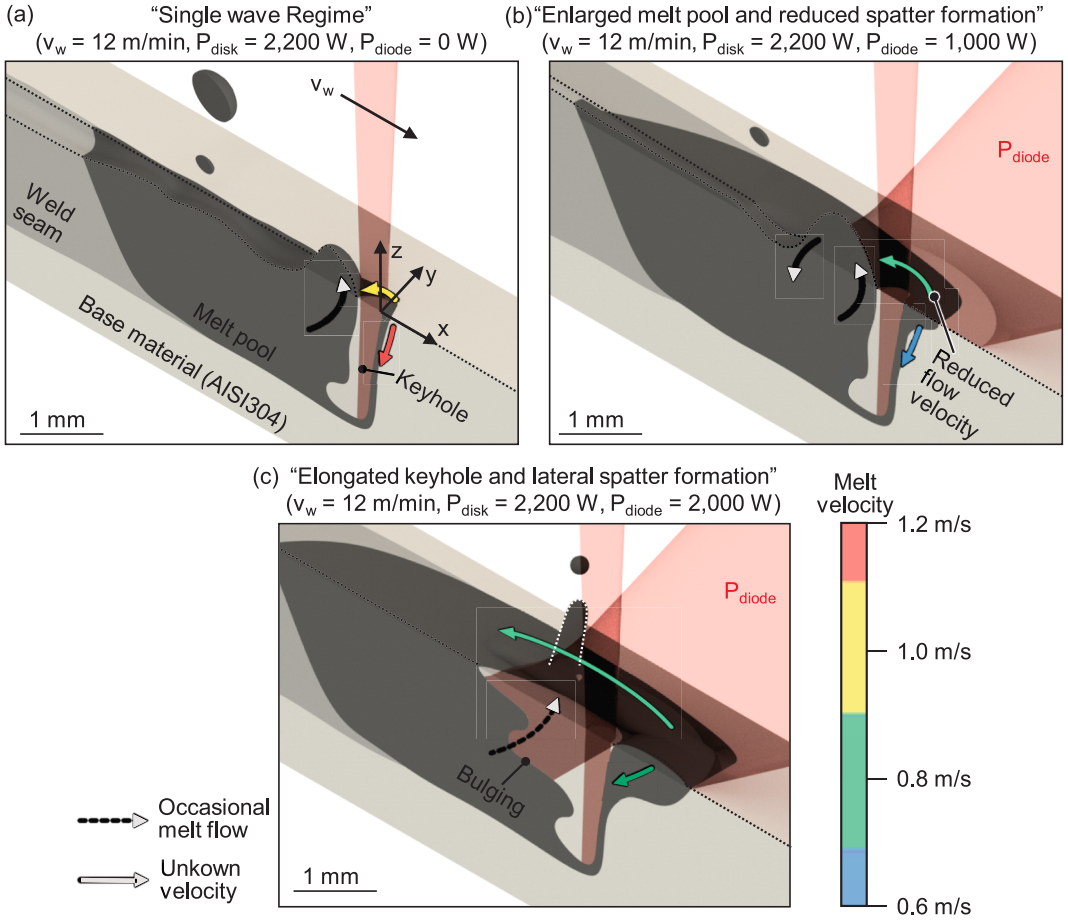


Fig. 21. Schematic illustrations for the welding speed 12 m/min; (a) Reference process without diode laser, (b) Increased melt pool width and reduced spatter formation, (c) Elongation of the keyhole and lateral spatter formation.

corresponding author. High-speed synchrotron radiation imaging data are available in [57].

CRediT authorship contribution statement

Christian Diegel: Writing – original draft, Software, Methodology, Investigation, Conceptualization. **Leander Schmidt:** Writing – review & editing, Methodology, Investigation, Funding acquisition, Conceptualization. **Klaus Schricker:** Writing – review & editing, Methodology, Funding acquisition, Conceptualization. **Marc Seibold:** Investigation. **Felix Zaiß:** Writing – review & editing, Methodology, Investigation. **Christian Hagenlocher:** Writing – review & editing, Methodology, Investigation, Funding acquisition, Conceptualization. **Christoph Spurk:** Resources. **Marc Hummel:** Resources. **Alexander Olowinsky:** Resources. **Felix Beckmann:** Resources. **Julian Moosmann:** Resources. **Thomas Graf:** Supervision, Project administration, Funding acquisition. **Jean Pierre Bergmann:** Writing – review & editing, Supervision, Project administration, Funding acquisition, Conceptualization.

Funding

Funded by the Deutsche Forschungsgemeinschaft (DFG, German Research Foundation) – 503306266. The presented investigations were carried out within the cooperation “Laser Meets Synchrotron” (https://www.laser-meets-synchrotron.de). The experimental setup and its operation were funded by the Deutsche Forschungsgemeinschaft e.V. (DFG, German Research Foundation) within the framework of the Collaborative Research Centre SFB1120-236616214 “Bauteilpräzision durch Beherrschung von Schmelze und Erstarrung in Produktionsprozessen”.

Declaration of competing interest

The authors declare that they have no known competing financial interests or personal relationships that could have appeared to influence the work reported in this paper.

Acknowledgments

The authors would like to thank Michaela Blum and Marcus Hopfeld from the Center of Micro- and Nanotechnologies (ZMN) (DFG RIsources reference: RI_00009), a DFG-funded core facility (Grant No. MU 3171/2-1 + 6-1, SCHA 632/19-1 + 27-1, HO 2284/4-1 + 12-1) at TU Ilmenau, for their support with the experiments concerning the chemical composition of the material used. We acknowledge Hereon (Geesthacht, Germany) and DESY (Hamburg, Germany), members of the Helmholtz Association HGF, for the provision of experimental facilities. Parts of this research were carried out at PETRA III. Data was collected using the high energy material science (HEMS) beamline P07 operated by Helmholtz-Zentrum Hereon. Beamtime was allocated for proposal BAG-20211050. We acknowledge support for the publication costs by the Open Access Publication Fund of the Technische Universität Ilmenau.

References

[1] R. Fabbro, Scaling laws for the laser welding process in keyhole mode, J. Mater. Process. Technol. 264 (2019) 346–351, https://doi.org/10.1016/j.jmatprotec.2018.09.027.
[2] U. Brauch, C. Röcker, T. Graf, M. Abdou Ahmed, High-power, high-brightness solid-state laser architectures and their characteristics, Appl. Phys. B 128 (2022) 58, https://doi.org/10.1007/s00340-021-07736-0.
[3] M.S. Khan, S. Ali, D. Westerbaan, W. Duley, E. Biro, Y.N. Zhou, The effect of laser impingement angle on the optimization of melt pool geometry to improve process stability during high-speed laser welding of thin-gauge automotive steels, J. Manuf. Process. 78 (2022) 242–253, https://doi.org/10.1016/j.jmapro.2022.04.022.
[4] A. Tadamalle, Y. Reddy, E. Ramjee, V. Reddy, Influence of welding speed on the melting efficiency of Nd: YAG laser welding, Adv. Prod. Eng. Manage. 9 (2014), https://doi.org/10.14743/APEM2014.3.182.
[5] S. Katayama, S. Tsukamotot, R. Fabbro, *Handbook of laser welding technologies*, Woodhead Publishing, 2013.
[6] L. Schmidt, S. Hickethier, K. Schricker, J.P. Bergmann, Low-spatter high speed welding by use of local shielding gas flows, Proceedings of SPIE LASE Conference 10911 (2019), https://doi.org/10.1117/12.2507024.
[7] C. Diegel, T. Mattulat, K. Schricker, L. Schmidt, T. Seefeld, J.P. Bergmann, P. Woizeschke, Interaction between local shielding gas supply and laser spot size on spatter formation in laser beam welding of AISI 304, Appl. Sci. 13 (2023), https://doi.org/10.3390/app131810507.
[8] J. Frostevarg, A.F.H. Kaplan, Undercuts in Laser Arc Hybrid Welding, Phys. Procedia 56 (2014) 663–672, https://doi.org/10.1016/j.phpro.2014.08.071.
[9] T.A. Mamvura, A.E. Paterson, D. Fanucchi, The impact of pipe geometry variations on hygiene and success of orbital welding of brewing industry equipment, J. Inst. Brew. 123 (2017) 81–97, https://doi.org/10.1002/jib.398.
[10] C. Tide, S.R. Harkin, G.G. Geesey, P.J. Bremer, W. Scholz, The influence of welding procedures on bacterial colonization of stainless steel weldments, J. Food Eng. 42 (1999) 85–96, https://doi.org/10.1016/S0260-8774(99)00109-0.
[11] Ghosh, K.S. *Foundation of Welding Technology*; PHI Learning Pvt. Ltd.: 2022.
[12] N. Speker, P. Haug, S. Feuchtenbeiner, T. Hesse, D. Havrilla, Spatter reduced high speed welding with disk lasers, Int. Congr. Appl. Lasers & Electro-Optics 2017 (2017) 407, https://doi.org/10.2351/1.5138146.
[13] F. Nagel, L. Brömme, J.P. Bergmann, Effects of two superimposed laser beams on spatter formation during laser welding of high alloyed steel, J. Laser Appl. 31 (2019) 022005, https://doi.org/10.2351/1.5040572.
[14] R. Fabbro, S. Slimani, F. Coste, F. Briand, Analysis of the various melt pool hydrodynamic regimes observed during cw Nd-YAG deep penetration laser welding, Proceedings of International Congress on Applications of Lasers & Electro-Optics 2007 (2007) 382–390, https://doi.org/10.2351/1.5061093.
[15] H. Hügel, T. Graf, *Materialbearbeitung mit Laser*, Springer Vieweg Wiesbaden 4 (2022).
[16] Weberpals, J. Nutzen und Grenzen guter Fokussierbarkeit beim Laserschweißen. Dissertation, Universität Stuttgart, Stuttgart, 2010.
[17] Schmidt, L.; Nagel, F.; Schricker, K.; Bergmann, J.P.; Bourgin, Y.; Wüster, J.; Sinzinger, S. Spritzerarmes Laserstrahlschweißen bei hohen Schweißgeschwindigkeiten unter Einsatz angepasster Intensitätsverteilungen. **2019**.
[18] Rominger, V. Untersuchungen der Prozessvorgänge bei Einschweißungen in Baustahl mit Lasern hoher Brillanz. Herbert Utz Verlag, 2017.
[19] H. Hügel, T. Graf, *Laser in der Fertigung: Grundlagen der Strahlquellen, Systeme, Fertigungsverfahren*, Vieweg+teubner 3 (2014).
[20] V. Rominger, T. Harrer, S. Keßler, H. Braun, F. Dorsch, F. Abt, M. Jarwitz, A. Heider, R. Weber, T. Graf, Formation mechanism of process instabilities and strategies to improve welding quality, Proceedings of International Congress on Applications of Lasers & Electro-Optics 2012 (2012) 565–573, https://doi.org/10.2351/1.5062509.
[21] J. Volpp, Formation mechanisms of pores and spatters during laser deep penetration welding, J. Laser Appl. 30 (2018) 012002, https://doi.org/10.2351/1.4993843.
[22] K.C. Mills, B.J. Keene, R.F. Brooks, A. Shirali, Marangoni effects in welding. *Philosophical transactions of the Royal Society of London. Series a: Mathematical*, Phys. Eng. Sci. 356 (1998) 911–925, https://doi.org/10.1098/rsta.1998.0196.
[23] T. Fuhrich, P. Berger, H. Hügel, Marangoni effect in laser deep penetration welding of steel, J. Laser Appl. 13 (2001) 178–186, https://doi.org/10.2351/1.1404412.
[24] A.F.H. Kaplan, J. Powell, Spatter in laser welding, J. Laser Appl. 23 (2011) 032005, https://doi.org/10.2351/1.3597830.
[25] P. Berger, R. Schuster, H. Hügel, T. Graf, Moving humps at the capillary front in laser welding, Proceedings of International Congress on Applications of Lasers & Electro-Optics 2010 (2010) 39–43, https://doi.org/10.2351/1.5062057.
[26] Beck, M. Modellierung des Lasertiefschweißens. Universität Stuttgart, Vieweg+Teubner: Stuttgart, 1996.
[27] V.V. Semak, J.A. Hopkins, M.H. McCay, T.D. McCay, Melt pool dynamics during laser welding, J. Phys. D Appl. Phys. 28 (1995) 2443, https://doi.org/10.1088/0022-3727/28/12/008.
[28] J. Wagner, A. Heider, R. Ramsayer, R. Weber, F. Faure, A. Leis, N. Armon, R. Susid, O. Tsiony, E. Shekel, T. Graf, Influence of dynamic beam shaping on the geometry of the keyhole during laser beam welding, Procedia CIRP 111 (2022) 448–452, https://doi.org/10.1016/j.procir.2022.08.185.
[29] N. Speker, P. Haug, S. Feuchtenbeiner, T. Hesse, D. Havrilla, BrightLine weld-spatter reduced high speed welding with disk lasers, SPIE LASE 10525 (2018), https://doi.org/10.1117/12.2287205.
[30] M. Möbus, P. Woizeschke, Laser beam welding setup for the coaxial combination of two laser beams to vary the intensity distribution, Weld. World 66 (2022) 471–480, https://doi.org/10.1007/s40194-021-01234-9.
[31] F. Nagel, M. Stambke, J.P. Bergmann, Reduction of spatter formation by superposition of two laser intensities, Int. Congr. Appl. Lasers & Electro-Optics 2016 (2016) 1502, https://doi.org/10.2351/1.5118549.
[32] M. Dal, R. Fabbro, An overview of the state of art in laser welding simulation, Opt. Laser Technol. 78 (2016) 2–14, https://doi.org/10.1016/j.optlastec.2015.09.015.
[33] M. Schaefer, S. Kessler, F. Fetzer, T. Graf, Influence of the focal position on the melt flow during laser welding of steel, J. Laser Appl. 29 (2017) 012010, https://doi.org/10.2351/1.4972098.
[34] A. Kurlov, A. Gusev, Tungsten carbides: structure, Properties and Application in Hardmetals 184 (2013).
[35] F. Abt, M. Boley, R. Weber, T. Graf, G. Popko, S. Nau, Novel X-ray system for in-situ diagnostics of laser based processes – first experimental results, Phys. Procedia 12 (2011) 761–770, https://doi.org/10.1016/j.phpro.2011.03.095.

[36] K. Schricker, C. Diegel, L. Schmidt, M. Seibold, H. Friedmann, F. Fröhlich, S. Eichler, Y. Chen, H. Requardt, A. Rack, J.P. Bergmann, Understanding the formation of "false friends" (hidden lack of fusion defects) in laser beam welding by means of high-speed synchrotron X-ray imaging, Weld. World (2023), https://doi.org/10.1007/s40194-023-01581-9.
[37] D.I.N.E.N. Norm, 10088-1: Nichtrostende Stähle - Teil 1, Verzeichnis Der Nichtrostenden Stähle. (2014).
[38] Jovic, G.; Bormann, A.; Pröll, J.; Niendorf, T.; Böhm, S. Impact of sulphur content on spattering and weld seam shape in steel specimens using modified side-gas application technique. *Proceedings of WLT Conf. Lasers in Manufacturing* **2021**.
[39] F. Zaiß, M. Haas, J. Powell, J. Wahl, C. Diegel, K. Schricker, J.P. Bergmann, M. Hummel, C. Spurk, A. Olowinsky, F. Beckmann, J. Moosmann, C. Hagenlocher, T. Graf, Reducing capillary depth fluctuations in high-speed laser welding of stainless steel using multi-core laser technology, Procedia CIRP 124 (2024) 413–417, https://doi.org/10.1016/j.procir.2024.08.144.
[40] Norm. DIN EN ISO 11146-1: Laser und Laseranlagen – Prüfverfahren für Laserstrahlabmessungen, Divergenzwinkel und Beugungsmaßzahlen. **2021.**
[41] M. Hummel, C. Hagenlocher, A. Haeusler, S. Hollatz, J. Lind, A. Olowinsky, A. Gillner, F. Beckmann, J. Moosmann, R. Weber, T. Graf, C. Häfner, Analysis on the influence of vapor capillary aspect ratio on pore formation in laser beam welding of aluminum, J. Mater. Process. Technol. 312 (2023) 117862, https://doi.org/10.1016/j.jmatprotec.2023.117862.
[42] C.A. Schneider, W.S. Rasband, K.W. Eliceiri, NIH image to ImageJ: 25 years of image analysis, Nat. Methods 9 (2012) 671–675, https://doi.org/10.1038/nmeth.2089.
[43] J.A. Seibert, J.M. Boone, K.K. Lindfors, Flat-field correction technique for digital detectors. *Proc*, SPIE 3336 (1998) 348–354, https://doi.org/10.1117/12.317034.
[44] N.M. Qureshi, U. Arrieta, C. Baudet, A. Cartellier, Y. Gagne, M. Bourgoin, Acceleration statistics of inertial particles in turbulent flow, The European Physical Journal B 66 (2008) 531–536, https://doi.org/10.1140/epjb/e2008-00460-x.
[45] S.M. Hartig, Basic image analysis and manipulation in imagej, Curr. Protoc. Mol. Biol. 102 (2013) 14.15.11-14.15.12, https://doi.org/10.1002/0471142727.mb1415s102.
[46] I.F. Sbalzarini, P. Koumoutsakos, Feature point tracking and trajectory analysis for video imaging in cell biology, J. Struct. Biol. 151 (2005) 182–195, https://doi.org/10.1016/j.jsb.2005.06.002.
[47] K. Mundra, T. Debroy, Calculation of weld metal composition change in high-power conduction mode carbon dioxide laser-welded stainless steels, Metall. Trans. B 24 (1993) 145–155, https://doi.org/10.1007/BF02657881.
[48] W.V. Ohnesorge, Die bildung von tropfen an düsen und die auflösung flüssiger strahlen, ZAMM - Journal of Applied Mathematics and Mechanics / Zeitschrift Für Angewandte Mathematik Und Mechanik 16 (1936) 355–358, https://doi.org/10.1002/zamm.19360160611.
[49] S.M. Robertson, A.F.H. Kaplan, J. Frostevarg, Material ejection attempts during laser keyhole welding, J. Manuf. Process. 67 (2021) 91–100, https://doi.org/10.1016/j.jmapro.2021.04.052.
[50] Q.V. Nguyen, R.H. Rangel, D. Dunn-Rankin, Measurement and prediction of trajectories and collision of droplets, Int. J. Multiph. Flow 17 (1991) 159–177, https://doi.org/10.1016/0301-9322(91)90013-S.
[51] L. Schmidt, R. Azizy, K. Schricker, C. Diegel, Y. Chen, A. Rack, J.P. Bergmann, Describing the effect of local gas flow on keyhole and melt flow dynamics utilizing high-speed synchrotron X-ray imaging and numerical simulation, Procedia CIRP 124 (2024) 553–558, https://doi.org/10.1016/j.procir.2024.08.173.
[52] A. Artinov, X. Meng, N. Bakir, Ö. Üstündağ, M. Bachmann, A. Gumenyuk, M. Rethmeier, The bulging effect and its relevance in high power laser beam welding, IOP Conf. Ser.: Mater. Sci. Eng. 1135 (2021) 012003, https://doi.org/10.1088/1757-899X/1135/1/012003.
[53] A.F.H. Kaplan, M. Mizutani, S. Katayama, A. Matsunawa, Mechanism of pore formation during keyhole laser spot welding. *Proc*, SPIE 4831 (2003) 186–191, https://doi.org/10.1117/12.497914.
[54] P. Berger, H. Hügel, Fluid dynamic effects in keyhole welding an attempt to characterize different regimes, Phys. Procedia 41 (2013) 216–224.
[55] A.F.H. Kaplan, Local flashing events at the keyhole front in laser welding, Opt. Lasers Eng. 68 (2015) 35–41, https://doi.org/10.1016/j.optlaseng.2014.12.019.
[56] I. Eriksson, J. Powell, A.F.H. Kaplan, Melt behavior on the keyhole front during high speed laser welding, Opt. Lasers Eng. 51 (2013) 735–740, https://doi.org/10.1016/j.optlaseng.2013.01.008.
[57] C. Diegel, L. Schmidt, K. Schricker, M. Seibold, F. Zaiß, C. Hagenlocher, C. Spurk, M. Hummel, A. Olowinsky, F. Beckmann, J. Moosmann, T. Graf, J.P. Bergmann, Supplementary Data for publication "Visualization and quantification of melt flow dynamics for laser welding with superimposed intensity distributions analyzed by synchrotron radiation imaging", DaRUS (2026) https://doi.org/10.18419/DARUS-5747.